Vision-Based Nonlinear Incremental Control for A Morphing Wing with Mechanical Imperfections

Sun, Bo; Mkhoyan, Tigran; Van Kampen, Erik Jan; Breuker, Roeland De; Wang, Xuerui

DOI
10.1109/TAES.2022.3175679

Publication date
2022

Document Version
Final published version

Published in
IEEE Transactions on Aerospace and Electronic Systems

Vision-Based Nonlinear Incremental Control for a Morphing Wing With Mechanical Imperfections

BO SUN, Student Member, IEEE
TIGRAN MKHOYAN, Student Member, IEEE
ERIK-JAN VAN KAMPEN
ROELAND DE BREUKER
XUERUI WANG, Member, IEEE
Delft University of Technology, Delft, The Netherlands

Morphing structures have acquired much attention in the aerospace community because they enable an aircraft to actively adapt its shape during flight, leading to fewer emissions and fuel consumption. Researchers have designed, manufactured, and tested a morphing wing named SmartX-Alpha, which can actively alleviate loads while achieving the optimal lift distribution. However, the widely existing mechanical imperfections can degrade the performance of the morphing wing and even lead to instabilities. To tackle these issues, this article proposes a vision-based adaptive control approach to actively compensate for mechanical imperfections. In this approach, an incremental model is constructed online to identify the system dynamics using servo commands and vision measurements, and then, nonlinear dynamic inversion control is applied based on the identified model. This data-driven control approach with visual feedback has been validated by real-world experiments on the SmartX-Alpha. The results demonstrate that the vision-based system combined with the proposed control methodology can actively compensate for mechanical imperfections with minimal adjustments to the actual system design. Compared to a controller that only uses a feedforward input-output mapping, this proposed approach improves the system performance and decreases the tracking errors by more than 62% despite disturbances. The results collectively demonstrate the effectiveness of the proposed control system, which sets a foundation for realizing morphing in next-generation aircraft.

Manuscript received 9 August 2021; revised 17 March 2022; released for publication 4 May 2022. Date of publication 19 May 2022; date of current version 6 December 2022.

DOI. No. 10.1109/TAES.2022.3175679

Refereeing of this contribution was handled by I. Hwang.

Authors' addresses: Bo Sun and Erik-Jan van Kampen are with the Department of Control and Operations, Faculty of Aerospace Engineering, Delft University of Technology, 2629HS Delft, The Netherlands, E-mail: (B.Sun-1@TUDelft.nl; E.vanKampen@tudelft.nl); Tigran Mkhoyan, Roeland De Breuker, and Xuerui Wang are with the Department of Aerospace Structures and Materials, Faculty of Aerospace Engineering, Delft University of Technology, 2629HS Delft, The Netherlands, E-mail: (T.Mkhoyan@tudelft.nl; r.debreuker@tudelft.nl; X.Wang-6@tudelft.nl). *(Corresponding author: Xuerui Wang.)*

I. INTRODUCTION

Active morphing can bring several benefits to conventional wing designs. Morphing wings have the potential to improve aircraft performance across the full flight envelope, by actively adapting the shape. Due to conflicting requirements [1], conventional wing designs generally can only be optimized for one single flight condition, such as cruise. To assess the benefits of morphing wings, the SmartX project [2] was initiated at the Delft University of Technology. An overactuated and oversensed wing prototype was developed for this project, named SmartX-Alpha, capable of seamless active wing morphing with six distributed translation-induced camber (TRIC) morphing modules [3].[1] Coupled with advanced nonlinear control methods, this wing has demonstrated the capability to actively reduce gust loads while actively maintaining an optimal lift distribution in a recent wind tunnel study [4].

However, due to the mechanical complexity and manufacturing imperfections, mechanical imperfections generally exist in aerospace systems, such as input saturation [5], friction [6], dead zone [7], and disturbances. These nonlinearities can largely degrade the system performance and lead to undesirable phenomena such as limit-cycle oscillations, flutter, and even divergence [7], [8]. Apart from these, backlash hysteresis is also observed in both wind tunnel tests and a design validation assessment with a digital image correlation (DIC) setup [4], which is caused by the nature of the morphing mechanism. This backlash effect diminishes the achievable morphing range and consequently reduces the aerodynamic control effectiveness of the wing. Instead of perfecting hardware, which is costly and nonadaptative, an alternative is to actively compensate for these hardware imperfections via software algorithms. However, as depicted in Fig. 1, the backlash output u is a function of not only the input u_c but also its derivative $\dot{u}_c$, which is fundamentally different from the other common nonlinearities that act directly on the actuation output. Consequently, the time-dependent hysteresis effect makes backlash compensation a challenging problem.

Conventional linear control methods, paired with the gain-scheduling technique, are not suitable for this task because the closed-loop stability and performance cannot be guaranteed in between the operational points [9]. For example, classic proportional-derivative control has been observed to result in limit-cycle oscillations in the presence of backlash [10]. There are also some adaptive control approaches designed for backlash such as [11] that employs an observer with adjustable parameters. However, they often rely on fixed structures and are limited for complex and variant nonlinearities [11]. Alternatively, some articles

[1]The project video can be found via [Online]. Available: https://www.youtube.com/watch?v=SdagIiYRWyA

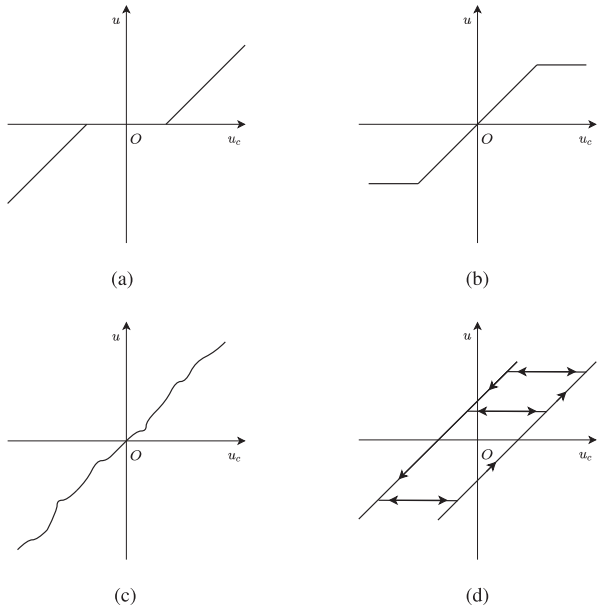

Fig. 1. Different types of mechanical imperfections. (a) Dead zone. (b) Saturation. (c) Disturbance. (d) Backlash.

approximately treat backlash as a dead zone [12] or disturbances [7], [13] and try to passively resist the unmodeled uncertain dynamics by the robustness of the controller, but their performance degrades heavily when the backlash phenomenon becomes severe.

Apart from the aforementioned methods, the nonlinear dynamic inversion (NDI)-based control is one of the most general and effective methods to cope with backlash compensation. It can entirely or partially cancel the system dynamics through dynamic inversion, reconstructing and recovering a linear mapping between the system inputs and outputs [9], [14]. NDI and its variants have been widely applied in the aerospace community [9], [14]–[16]. To compensate for the backlash hysteresis in the NDI framework, researchers have attempted to employ analytical compensation [17], adaptive compensation using a fixed structure with variable parameters [18], [19], or intelligent compensation with neural networks [10], [20] and fuzzy logic [6], [21]. In these existing publications, the backlash dynamics has to be standard and is assumed known or unknown but invariant, and global regulation is adopted for inversion. However, owing to uncertainties and disturbances, the backlash nonlinearity in the SmartX-Alpha wing is not always standard and invariant, which leads to the invalidation when embedded in a real application. The limitations in the existing methods motivate our research in investigating online active compensation methods with no need for known or invariant dynamics.

To actively compensate for mechanical imperfections, online identification techniques are necessary such that the controller can adapt to constantly changing flight conditions and environments. The classic grey-box-based observer [14] that requires full state feedback is not valid for the SmartX-Alpha morphing wing system because of the unavailability of internal states (e.g., the states of the nonlinear backlash and aeroelastic dynamics). Therefore, output-feedback (OPFB) identification and control methods are required. Some identification methods rely on the global model, in which nonlinear approximators like neural networks [22], [23] are often involved. However, these methods usually require large amount of data and sometimes perform not well enough for online applications [24]. Therefore, a precise online identification technique that requires fewer samples and less computation power is desired. In [25], an online OPFB identification method, producing the so-called incremental model (IM), is proposed based on the locally linearized dynamics, which allows for the OPFB scheme using only input-output data. Combined with intelligent control methods, the incremental model has successfully been applied to various aerospace systems [24]–[26]. Nevertheless, the effectiveness of the IM in the real-world system has not been validated yet. Considering the demand for actively compensating for mechanical imperfections, an adaptive control method combining the IM and the NDI control approach will be designed in this article, yielding incremental model-based nonlinear dynamic inversion (IM-NDI). The proposed control approach is competent at OPFB tracking control while online identifying the system dynamics regardless of mechanical imperfections and external disturbances.

To enable a real-time mechanical imperfection compensation in the real world, the controller has to know the shape of the morphing wing in real time. Furthermore, our study aims to provide a solution for an existing imperfect mechanical design, preferably imposing minimal adjustments to the hardware. In this article, we propose to accomplish this task by vision-based control. As compared to conventional sensors, such as strain gauges and accelerometers, computer vision has higher scalability, implementation flexibility, and robustness towards temperature variations [27]. In our previous research, vision-based tracking has demonstrated its effectiveness in flexible and morphing system shape estimations, featured by its noninvasive and model-free natures [28]. Coupled with nonlinear filtering techniques, a vision-based tracking system can be retro-fitted to an existing wing design and provide the capability to measure wing vibrations in the presence of gusts [28]. This setup can also be used as a stabilization system for flapping-wings [29], obstacle avoidance for UAVs [30], and flight maneuvering tracking [31]. Vision-based control can also benefit truss-based morphing mechanisms with a large number of actuators [32], which is an active research field in the robotics field [33], [34].

The main contributions of this article are summarized as follows:

1) The methodology and real-world implementation techniques for the proposed vision-based IM-NDI to actively compensate for mechanical imperfections (particularly for backlash hysteresis) are validated in morphing wing experiments.

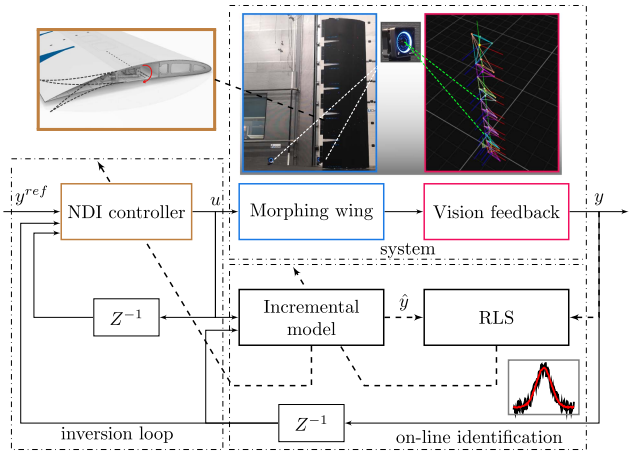

Fig. 2. Architecture of the IM-NDI controller, where the solid lines denote the signal flows and the dashed lines represent the parameter update paths.

2) The vision-based feedback using distributed infrared (IR) sensors is for the first time proposed for and applied to the morphing wing to enable a robust and precise measurement with high reliability, maintainability, scalability, and sampling frequency.
3) The online identification effectiveness of the data-driven extended incremental model applied to the OPFB problem is proved in theory and demonstrated in real-world experiments.

The rest of this article is organized as follows. Section II introduces the IM-NDI approach. Section III describes the vision-based control system. The experiment study is presented in Section IV. Finally, Section V concludes this article.

II. IM-NDI CONTROLLER DESIGN

This section first presents the derivation of the IM regarding the input-output data, and then introduces the recursive least squares (RLS) algorithm to identify the parameters of the IM online. After that, an NDI control method based on the IM is designed. The layout of the IM-NDI controller is depicted in Fig. 2.

A. Incremental Model

Consider a nonlinear multi-input–multi-output (MIMO) system described by

$$\begin{aligned} \dot{x}(t) &= f(x(t), u(t)) \\ y(t) &= h(x(t)) \end{aligned} \tag{1}$$

where $x \in \mathbb{R}^n$, $u \in \mathbb{R}^m$, and $y \in \mathbb{R}^p$ are the system state vector, control input vector, and measurable output state vector, respectively. $f : (\mathbb{R}^n, \mathbb{R}^m) \to \mathbb{R}^n$ and $h : \mathbb{R}^n \to \mathbb{R}^p$ are assumed to be Lipschitz continuous on their domains. The nonlinear system is assumed to be both controllable and observable.

The IM is constructed based on linearization and discretization techniques. To retain sufficiently high precision, the following assumption is required, such that given a sufficiently small sampling interval Δt, errors caused by linearization and discretization can be bounded within a small vicinity of zero:

ASSUMPTION 1 ([24]) The sampling frequency is sufficiently high, and the system dynamics are relatively slow time-varying.

With a sampling frequency of 100 Hz, Assumption 1 holds in aerospace applications [9], [35]. Experimental results have shown that 60 Hz is sufficient for this morphing wing control problem.

Before discretization, we first assume that the system is first-order continuous with respect to time, and therefore, we can approximately linearize the system dynamics (1) at around a time instant t_0, by taking the first-order Taylor series expansion as follows:

$$\begin{aligned} \dot{x}(t) &= \dot{x}(t_0) + F[x(t_0), u(t_0)]\Delta x \\ &\quad + G[x(t_0), u(t_0)]\Delta u + O(\Delta x^2, \Delta u^2) \\ y(t) &= y(t_0) + H[x(t_0)]\Delta x + O(\Delta x^2) \end{aligned} \tag{2}$$

where $F[x(t_0), u(t_0)] = \frac{\partial f^{\mathsf{T}}[x(t),u(t)]}{\partial x(t)}|_{x(t_0),u(t_0)} \in \mathbb{R}^{n\times n}$, $G[x(t_0), u(t_0)] = \frac{\partial f^{\mathsf{T}}[x(t),u(t)]}{\partial u(t)}|_{x(t_0),u(t_0)} \in \mathbb{R}^{n\times m}$, and $H[x(t_0)] = \frac{\partial h^{\mathsf{T}}[x(t)]}{\partial x(t)}|_{x(t_0)} \in \mathbb{R}^{p\times n}$ are bounded due to the Lipschitz continuity of f and h in (1), respectively. $\Delta x = x(t) - x(t_0)$, $\Delta u = u(t) - u(t_0)$. $O(\Delta x^2, \Delta u^2)$ and $O(\Delta x^2)$ denote higher-order terms.

Since the controller is designed based on the identified dynamics, the higher order terms can perturb the closed-loop performance. Nevertheless, as claimed in [9], these higher order terms satisfy

$$\begin{aligned} \lim_{\Delta t\to 0} ||O(\Delta x^2, \Delta u^2)||_2 = 0 \quad \forall x \in \mathbb{R}^n \quad \forall u \in \mathbb{R}^m \\ \lim_{\Delta t\to 0} ||O(\Delta x^2)||_2 = 0 \quad \forall x \in \mathbb{R}^n \end{aligned} \tag{3}$$

where $\Delta t = t - t_0$ is the sampling interval. As demonstrated in (3), the norm values of the higher order terms approach zero under Assumption 1. Besides, (3) also implies that $\forall \bar{O} > 0$, $\exists \overline{\Delta t} > 0$ such that for all $0 < \Delta t \le \overline{\Delta t}$ $\forall x \in \mathbb{R}^n$ $\forall u \in \mathbb{R}^m$ $\forall t \ge t_0$, $||O(\Delta x^2, \Delta u^2)||_2 \le \bar{O}$ and $||O(\Delta x^2)||_2 \le \bar{O}$, i.e., there exists a Δt that guarantees the boundedness of the higher-order terms. Furthermore, the IM adopts a local linearization technique such that the linearization errors will not accumulate. Consequently, the two higher order terms in (2) are omitted hereafter in the control design process for convenience.

Then, an IM can be utilized to approximately represent (2) using the Euler method accordingly:

$$\begin{aligned} \Delta x_{t+1} &\approx (I_n + F_{t-1}\Delta t)\Delta x_t + G_{t-1}\Delta t\,\Delta u_t \\ \Delta y_{t+1} &\approx H_t \Delta x_{t+1} \end{aligned} \tag{4}$$

where the subscript t stands for the current sampling time instant and I_n denotes an n-dimensional identity matrix. $F_{t-1} = \frac{\partial f^{\mathsf{T}}(x,u)}{\partial x}|_{x_{t-1},u_{t-1}} \in \mathbb{R}^{n\times n}$, $G_{t-1} = \frac{\partial f^{\mathsf{T}}(x,u)}{\partial u}|_{x_{t-1},u_{t-1}} \in \mathbb{R}^{n\times m}$, and $H_t = \frac{\partial h^{\mathsf{T}}(x)}{\partial x}|_{x_t} \in \mathbb{R}^{p\times n}$, respectively, denote the system transition matrix, the input distribution

matrix, and the observation matrix of the discretized system. For simplicity, we denote $A_{t-1} \triangleq I_n + F_{t-1}\Delta t$ and $B_{t-1} \triangleq G_{t-1}\Delta t$ hereafter.

Inspired by the work in [24], [25], and [36], the incremental dynamics at the current time instant t can be represented using previous data sequences on a time horizon $[t-N, t-1]$ as

$$\begin{aligned} \Delta x_t &\approx \tilde{A}_{t-2,t-N-1}\Delta x_{t-N} + U_N \overline{\Delta u}_{t-1,N} \\ \overline{\Delta y}_{t,N} &\approx V_N \Delta x_{t-N} + T_N \overline{\Delta u}_{t-1,N} \end{aligned} \tag{5}$$

where $\overline{\Delta u}_{t-1,N} = [\Delta u_{t-1}^{\mathsf{T}}, \Delta u_{t-2}^{\mathsf{T}}, \ldots, \Delta u_{t-N}^{\mathsf{T}}]^{\mathsf{T}} \in \mathbb{R}^{Nm}$, $\overline{\Delta y}_{t,N} = [\Delta y_t^{\mathsf{T}}, \Delta y_{t-1}^{\mathsf{T}}, \ldots, \Delta y_{t-N+1}^{\mathsf{T}}]^{\mathsf{T}} \in \mathbb{R}^{Np}$, $\tilde{A}_{a,b} = \prod_{i=a}^{b} A_i$. The controllability matrix is $U_N = [B_{t-2}, A_{t-2}B_{t-3}, \ldots, \tilde{A}_{t-2,t-N}B_{t-N-1}] \in \mathbb{R}^{n\times mN}$, while $V_N = [(H_{t-1}\tilde{A}_{t-2}, t-N-1)^{\mathsf{T}}, (H_{t-2}\tilde{A}_{t-3,t-N-1})^{\mathsf{T}}, \ldots, (H_{t-N}A_{t-N-1})^{\mathsf{T}}]^{\mathsf{T}} \in \mathbb{R}^{pN\times n}$ is the observability matrix.

$$T_N = \begin{bmatrix} H_{t-1}B_{t-2} & H_{t-1}A_{t-2}B_{t-3} & \cdots & H_{t-1}\tilde{A}_{t-2,t-N}B_{t-N-1} \\ 0 & H_{t-2}B_{t-3} & \cdots & H_{t-2}\tilde{A}_{t-3,t-N}B_{t-N-1} \\ \vdots & \vdots & \ddots & \vdots \\ 0 & 0 & \cdots & H_{t-N}B_{t-N-1} \end{bmatrix} \in \mathbb{R}^{pN\times mN}.$$

For OPFB scenarios, only the output y_t instead of the full state x_t can be measured. To determine system transitions with input-output observations, the following assumptions are required.

ASSUMPTION 2 ([35]) The linearization and discretization do not change the property of controllablity and observability of the original system described by (1), i.e., (A_{t-1}, B_{t-1}) is controllable and (A_{t-1}, H_t) is observable.

ASSUMPTION 3 ([35]) The deduced system (4) can be regarded deterministic within the range of M time steps, where $M \geq n/p$.

ASSUMPTION 4 During the identification and control process, the persistent excitation (PE) condition [37] is always satisfied.

Assumptions 2 and 3 are proposed based on Assumption 1. Both of them are necessary for the fidelity of the identified local model. According to Assumptions 2–4, the system is observable, locally deterministic, and persistently excited. Therefore, there must exist an observability index K, such that the column rank of the observability matrix V_N satisfies $\text{rank}(V_N) < n$, $\forall N < K$, and $\text{rank}(V_N) = n$, $\forall N \geq K$. Note that K satisfies $n/p \leq K \leq M$.

Let $N \leq K \leq M$, and there exists a matrix $\bar{N} \in \mathbb{R}^{n\times pN}$ such that

$$\tilde{A}_{t-2,t-N-1} = \bar{N}V_N. \tag{6}$$

Since V_N has a full column rank, thus we can obtain its left inverse V_N^+ by

$$V_N^+ = (V_N^{\mathsf{T}}V_N)^{-1}V_N^{\mathsf{T}} \tag{7}$$

so that

$$\bar{N} = \tilde{A}_{t-2,t-N-1}V_N^+ + Z(I_n - V_N V_N^+) \equiv \bar{N}_0 + \bar{N}_1 \tag{8}$$

holds for any matrix Z, with $\bar{N}_0$ denoting the minimum norm operator and $P(\mathbb{R}^{\perp}(V_N)) = I_n - V_N V_N^+$ being the projection onto a range perpendicular to V_N [36].

Inspired by [25], the following lemma is proposed to demonstrate how to reconstruct the unmeasurable system states from the input-output data:

LEMMA 1 Given Assumptions 2–4, the unmeasurable internal states x_t can be reconstructed uniquely in terms of the previous input-output sequences by

$$\Delta x_t \approx \bar{N}_0 \overline{\Delta y}_{t,N} + (U_N - \bar{N}_0 T_N)\overline{\Delta u}_{t-1,N} \tag{9}$$

where N satisfies $n/p \leq K \leq N \leq M$.

PROOF See Appendix A. □

Lemma 1 provides a deterministic relationship between the previous measured data and unmeasured states over a long-enough time horizon, which illustrates the rationality and validity of the IM. However, the matrices representing the system dynamics (A_{t-1}, B_{t-1}, H_t, etc.) have to be known.

Therefore, in the next step, a direct mapping from the previous input-output data to the future output data regardless of the inner state is constructed based on the IM. This model utilizing the stored data sequences is named as the extended IM, and is presented in the following theorem.

THEOREM 1 Under Assumptions 2–4, then given the measured input-output data over a long-enough time horizon, $[t-N+1, t]$, $N \geq n/p$, the output increment Δy_{t+1} can uniquely be determined as follows:

$$\Delta y_{t+1} \approx \underline{F}_t \overline{\Delta y}_{t,N} + \underline{G}_t \overline{\Delta u}_{t,N} \tag{10}$$

where $\underline{F}_t \in \mathbb{R}^{p\times Np}$ and $\underline{G}_t \in \mathbb{R}^{p\times Nm}$, respectively, denotes the transition matrix and the input distribution matrix of this extended discrete system.

PROOF The following proof is adapted from [25]. According to (5), the following approximation holds:

$$\overline{\Delta y}_{t-1,N} \approx \bar{V}_N \Delta x_{t-N} + \bar{T}_N \overline{\Delta u}_{t-1,N} \tag{11}$$

where $\bar{V}_N = [(H_{t-2}\tilde{A}_{t-3,t-N-1})^{\mathsf{T}}, (H_{t-3}\tilde{A}_{t-4,t-N-1})^{\mathsf{T}}, \ldots, H_{t-N-1}^{\mathsf{T}}]^{\mathsf{T}} \in \mathbb{R}^{pN\times n}$ and

$$\bar{T}_N = \begin{bmatrix} 0 & H_{t-2}B_{t-3} & H_{t-2}A_{t-3}B_{t-4} & \cdots & H_{t-2}\tilde{A}_{t-3,t-N}B_{t-N-1} \\ 0 & 0 & H_{t-3}B_{t-4} & \cdots & H_{t-3}\tilde{A}_{t-4,t-N}B_{t-N-1} \\ \vdots & \vdots & \vdots & \ddots & \vdots \\ 0 & 0 & 0 & \cdots & H_{t-N}B_{t-N-1} \\ 0 & 0 & 0 & 0 & 0 \end{bmatrix} \in \mathbb{R}^{pN\times mN}.$$

Since the system is fully observable, when $N \geq n/p$, $\bar{V}_N$ also has a full column rank, and its left inverse is given by:

$$\bar{V}_N^+ = (\bar{V}_N^{\mathsf{T}}\bar{V}_N)^{-1}\bar{V}_N^{\mathsf{T}} \tag{12}$$

By left-multiplying $\bar{V}_N^+$ to (11) and substituting the resulted Δx_{t-N} into (5) and then the resulted Δx_t into (4), the dynamics that maps the previous measured data to the output can be obtained:

$$\begin{aligned}\Delta y_t &\approx H_{t-1}\tilde{A}_{t-2,t-N-1}\bar{V}_N^+\overline{\Delta y}_{t-1,N}\\ &\quad+(H_{t-1}U_N - H_{t-1}\tilde{A}_{t-2,t-N-1}\bar{V}_N^+\bar{T}_N)\overline{\Delta u}_{t-1,N}\\ &= \underline{F}_{t-1}\overline{\Delta y}_{t-1,N} + \underline{G}_{t-1}\overline{\Delta u}_{t-1,N}. \end{aligned} \tag{13}$$

By comparing (10) and (13), it can be found that they have the same representation but are for different time instants. This completes the proof. □

In this way, the original nonlinear continuous system is approximately transformed into a new locally linear discrete system. The $\underline{F}_t$ and $\underline{G}_t$ in the extended incremental model (10) will be identified online using the RLS algorithm presented in the next section.

B. Online Identification With the RLS Algorithm

An RLS algorithm is introduced in this section. Rewrite (10) in a row-by-row form as follows:

$$\Delta y_{t+1}^{\mathsf{T}} \approx \begin{bmatrix}\overline{\Delta y}_{t,N}^{\mathsf{T}} & \overline{\Delta u}_{t,N}^{\mathsf{T}}\end{bmatrix}\cdot\begin{bmatrix}\underline{F}_t^{\mathsf{T}}\\ \underline{G}_t^{\mathsf{T}}\end{bmatrix}. \tag{14}$$

Denote $\bar{z}_t = [\overline{\Delta y}_{t,N}^{\mathsf{T}}, \overline{\Delta u}_{t,N}^{\mathsf{T}}]^{\mathsf{T}} \in \mathbb{R}^{N(p+m)\times 1}$ as the input information of the extended IM identification, and $\underline{\Theta}_t = [\underline{F}_t, \underline{G}_t]^{\mathsf{T}} \in \mathbb{R}^{N(p+m)\times p}$ as the matrix to be determined.

According to Lemma 1 and Theorem 1, data sequences from at least n/p time instants are required. Hence, a sliding window technique [24], [35] is employed to store sufficient measured data for online identification, with the data window width N satisfying $N \geq n/p$.

The main procedure of the RLS algorithm is presented as follows [35], [38]:

$$\Delta\hat{y}_{t+1}^{\mathsf{T}} = \bar{z}_t^{\mathsf{T}}\hat{\underline{\Theta}}_t \tag{15}$$

$$\epsilon_t = \Delta y_{t+1}^{\mathsf{T}} - \Delta\hat{y}_{t+1}^{\mathsf{T}} \tag{16}$$

$$\hat{\underline{\Theta}}_{t+1} = \hat{\underline{\Theta}}_t + \frac{\underline{\mathrm{Cov}}_t\bar{z}_t}{\gamma_{\mathrm{RLS}} + \bar{z}_t^{\mathsf{T}}\underline{\mathrm{Cov}}_t\bar{z}_t}\epsilon_t \tag{17}$$

$$\underline{\mathrm{Cov}}_{t+1} = \frac{1}{\gamma_{\mathrm{RLS}}}\left(\underline{\mathrm{Cov}}_{t-1} - \frac{\underline{\mathrm{Cov}}_{t-1}\bar{z}_t\bar{z}_t^{\mathsf{T}}\underline{\mathrm{Cov}}_{t-1}}{\gamma_{\mathrm{RLS}} + \bar{z}_t^{\mathsf{T}}\underline{\mathrm{Cov}}_{t-1}\bar{z}_t}\right) \tag{18}$$

where $\hat{y}_{t+1}$ and $\hat{\underline{\Theta}}_t$ denote the estimated and approximated values of y_{t+1} and $\underline{\Theta}_t$, respectively; $\epsilon_t \in \mathbb{R}^p$ is the prediction error; $\underline{\mathrm{Cov}}_t \in \mathbb{R}^{(p+m)M\times(p+m)M}$ denotes the symmetric and positive definite estimation covariance matrix; $\gamma_{\mathrm{RLS}} \in (0, 1]$ is the forgetting factor.

Assumptions 1 and 3 imply that in a certain time horizon $\mathscr{A} = [t_0, t]$, where $N \leq t - t_0 \leq M < \infty$. The slowly varying extended system dynamics can be approximated by a linear model with constant pending parameters. Hence, based on the following assumption, the locally approximate convergence of the RLS algorithm is analyzed.

ASSUMPTION 5 ([24]) For the locally linear system (10), in the local domain $\mathscr{A}$, the measured data $\bar{z}_{t_0}, \ldots, \bar{z}_t$ constitute the samples of an ergodic process, such that the time average is valid. The unmodeled dynamics noises within one sliding window are formulated as a zero-mean white noise vector as

$$\Delta y_{t+1}^{\mathsf{T}} = \bar{z}_t^{\mathsf{T}}\underline{\Theta} + e_{o,t} \tag{19}$$

where $\underline{\Theta}$ is the locally optimal matrix, and $e_{o,t}$ is the equivalent plant noise independent of the samples $\bar{z}_t$.

THEOREM 2 If Assumptions 1–5 hold, and the RLS algorithm is conducted obeying (15)–(18), then the approximate augmented matrix $\hat{\underline{\Theta}}_t$ shows the trend of converging to the locally optimal matrix $\underline{\Theta}$.

PROOF See Appendix B. □

C. NDI Control

It is noteworthy that the identification is conducted online such that the IM can adapt to the variations and therefore reflect the system dynamics in real time. The following NDI controller is designed based on the adaptive IM and consequently has the capability to adapt online.

Define $e = y - y^{\mathrm{ref}}$ as the tracking error between the system output y and the reference signal y^{ref}. It is clear that given a Lyapunov function $J = e^2$, the tracking error dynamics is stable, when the following equation holds:

$$\dot{e} = \dot{y} - \dot{y}^{\mathrm{ref}} = -k_p e - k_d\dot{e} \tag{20}$$

where $k_p > 0$ and $k_d > 0$ are control parameters.

Discretizing (20) in the same way of (4) yields

$$\frac{\Delta e_{t+1}}{\Delta t} = \frac{\Delta y_{t+1}}{\Delta t} - \frac{\Delta y_{t+1}^{\mathrm{ref}}}{\Delta t} = -k_p e_t - k_d\frac{e_t - e_{t-1}}{\Delta t} \tag{21}$$

where $\Delta e_{t+1} = e_{t+1} - e_t$ and $\Delta y_{t+1}^{\mathrm{ref}} = y_{t+1}^{\mathrm{ref}} - y_t^{\mathrm{ref}}$.

The derivative of the reference signal is assumed to be slow-varying, i.e., $\Delta y_{t+1}^{\mathrm{ref}}/\Delta t \approx \Delta y_t^{\mathrm{ref}}/\Delta t$. Substituting the incremental model (10) yields

$$\underline{F}_t\overline{\Delta y}_{t,N} + \underline{G}_t\overline{\Delta u}_{t,N} - \Delta y_t^{\mathrm{ref}} \approx -k_p\Delta t e_t - k_d\Delta e_t. \tag{22}$$

With the identified system matrices $\hat{\underline{F}}_t$ and $\hat{\underline{G}}_t$, the control law is derived from (22) as

$$\begin{aligned}u_t \approx\ & u_{t-1} + \hat{\underline{G}}_{11,t}^{-1}(\Delta y_t^{\mathrm{ref}} - \hat{\underline{F}}_t\overline{\Delta y}_{t,N}\\ &- \hat{\underline{G}}_{12,t}\overline{\Delta u}_{t-1,N-1} - k_p\Delta t e_t - k_d\Delta e_t)\end{aligned} \tag{23}$$

where $\hat{\underline{G}}_{11,t} \in \mathbb{R}^{p\times m}$ and $\hat{\underline{G}}_{12,t} \in \mathbb{R}^{p\times(N-1)m}$ are partitioned matrices from $\hat{\underline{G}}_t$.

REMARK 1 Satisfying the PE condition is essential for both theoretical deduction and experimental implementation. A common approach to ensure the satisfaction of the PE condition is adding exploration noise to the control command [24], [25], such that even at a steady status, there is small vibration that does not affect the performance in general but can excite the system. In practice, it could be easier to satisfy the PE condition because there always exist noises and disturbances in the real world, which actually play the same role as the exploration noise.

REMARK 2 Although Assumption 4 and Remark 1 are given, in some practical situations, some elements of $\hat{G}_{11,t}$ can have too small values. Therefore, for the real-world implementation, lower bounds are set for these elements to guarantee the invertibility of $\hat{G}_{11,t}$ and to avoid aggressive control increments.

REMARK 3 Input constraints are imposed on the u_t calculated by (23). It is also feasible to explicitly consider input constraints while solving (22) following our previous research in [4].

It is noteworthy that the proposed IM-NDI is fundamentally different from the well-known incremental control (including incremental NDI, incremental backstepping, incremental sliding model control) in the literature [9], [16], [39]. First of all, the state-of-the-art incremental control methods only depend on the information (state derivatives and control input) of the previous single time step, whereas IM-NDI can make use of the information of previous N time steps. Consequently, IM-NDI is more applicable for solving hysteresis effects and is more robust. Second, the state-of-the-art incremental control methods normally neglect the state variation related term [9], whereas this neglection is abandoned in IM-NDI, further enhancing its robustness. Third, prior knowledge of the control effectiveness is normally required in the state-of-the-art incremental control methods, while the proposed IM-NDI method does not need any prior knowledge of system dynamics. This simplifies the experimental implementation and empowers IM-NDI with swift online adaptation ability.

III. VISION-BASED CONTROL

A crucial aspect of implementing a control strategy to compensate for mechanical imperfections is an accurate knowledge of the morphing wings' shape. In particular, the variable of interest to the controller is the local vertical displacement of the wing trailing-edge with respect to a body-fixed coordinate system. In a previous study, a morphing wing concept, utilizing the distributed TRIC has been described [3]. This design has a relatively stiff wing box and a flexible morphing trailing edge. A body-fixed coordinate system $\mathcal{F}_B$ is chosen to be near the root of the wing in the wing box section, with an origin O_B. The displacement of the trailing edge, denoted as $\boldsymbol{z} = [z_1, z_2, \ldots, z_{12}]^{\mathsf{T}}$ along 12 stations of the span is reconstructed in the $\mathcal{F}_B$ frame, from a camera-fixed frame $\mathcal{F}_C$ in real time, by means of vision-based tracking. Two locations in each of the six modules are tracked and fed back to the controller. The experimental setup is shown in Fig. 3. A concise overview of the vision-based tracking pipeline is shown in Fig. 4 and explained in the following sections.

A. Apparatus

The experimental apparatus is shown in Fig. 3. The system consists of a morphing wing with six distributed TRIC morphing modules placed in the Open Jet Facility (OJF)

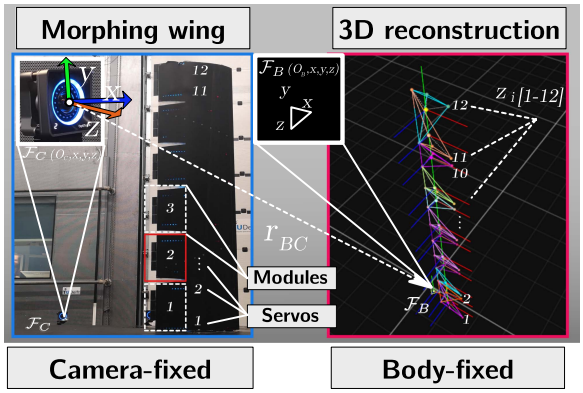

Fig. 3. Experimental apparatus with vision-based control components.

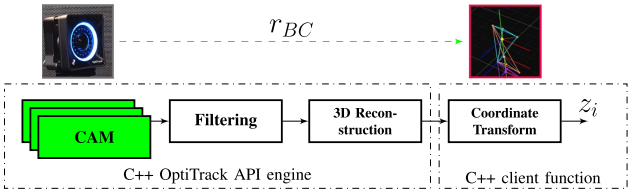

Fig. 4. Concise vision-based tracking pipeline.

wind tunnel facility of the Delft University of Technology. Each module is actuated by two embedded servos [3]. An array of IR light-emitting diodes (LEDs) are installed on the wing bottom surface, in the nonmorphing wing-box and the morphing trailing-edge modules. Four IR markers per module (24 in total) with another three markers defining the body-fixed reference frame are tracked by five Prime^{x}41 4.1 megapixel IR cameras at a frame rate of 250 frames per second (FPS) [41]. The deflections of the morphing flaps are reconstructed in real time with a reconstruction algorithm.

The intensity of IR has been adjusted to approximately 20 % and tuned to the obtain best tracking performance. Image segmentation and filtering are applied to further improve the tracking, which will be discussed in Section III-B.

B. Processing Framework

A 3-D reconstruction procedure is required to transform the measured marker correspondence $x_1, x_2, \ldots, x_n$ detected in the image frame, u, v, to a 3-D world coordinates defined in the camera fixed reference frame, $\mathcal{F}_C$. Segmentation and filtering are applied to the raw images in order to obtain the binary mask with marker locations in the image frames for each individual camera. The filtering consists of image threshold filtering and morphological image transformations [42] to improve the segmentation of distinct LED markers. An example of similar segmentation and filtering approach is presented in [28]. Active adjustment of the IR brightness was needed to prevent two or more markers from merging into a single blob for far away camera views.

In a previous study in OJF, a 3-D reconstruction approach with a stereo-camera setup was developed, which showed sensitivity to camera calibration due to the adverse environmental condition in the wind tunnel (flow conditions and mechanical vibrations) [28]. A generally suitable approach to improve the tracking accuracy and add redundancy to the tracking system is a multicamera (>2) setup [43]. Therefore, to improve robustness against calibration drift developed over time, a five-camera setup was used in this study.

The n-view 3-D reconstruction problem is concerned with finding the optimal estimation of an object $\hat{X}$ in a 3-D global coordinate frame (i.e., locations in the x-, y-, and z-axes), which is observable in noisy $\bar{x}_1, \bar{x}_2, \ldots, \bar{x}_n$ points correspondence in n camera views. The point correspondences $\bar{x}_i$ are generally defined by markers in u, v coordinates of a 2-D image plane. Back-projecting the 3-D point onto the respective camera views, a minimization problem can be defined to find the reprojection error, $E = \sum_{k=1}^{n} ||x_k - \bar{x}_k||^2$, and solved by an expanded linear system of equations similar to singular value decomposition in a direct linear transform (DLT) procedure [44]. Global optimization methods can be applied, such as algebraic, matrix inequality, and the $\mathcal{L}_\infty$ approach [45]. The development of a particular n-view triangulation method is not considered in this study. To perform the 3-D point cloud reconstruction in real time, a proprietary reconstruction engine is used by OptiTrack API [46]. All the applications for processing, reconstructing, and accessing the data are written in low-level C++ programming language for best performance. Multicamera calibration is performed by wandering process, resulting in an average calibration error of 0.25 mm for all cameras. The accuracy of a similar setup has been verified in [47]. It is noteworthy that the OptiTrack setup is not ready for onboard in-flight operation yet. Instead, our previous research has developed a fuselage/wing-mounted non-IR based camera tracking setup, whose effectiveness has been verified by wind tunnel experiments and real-world flight tests [28]. Nevertheless, the wing shape algorithms (including filtering, 3-D reconstruction, and coordination transformations) for these two setups are analogous.

The final step in the vision-based tracking pipeline is a coordinate system transformation from the global camera-fixed coordinate system, $\mathcal{F}_C$ with an origin O_C, to the body-fixed coordinate system, $\mathcal{F}_B$ with an origin O_B. This transformation is needed to express the relative deflections of the trailing-edge modules z_i with respect to the baseline unmorphed shape. The coordinate frames and their respective origins, located at approximately 2 m away, are connected by a vector r_{BC}, as shown in Fig. 3. The transformation $\mathcal{F}_C \rightarrow \mathcal{F}_B$ is achieved by a translation, followed by three-axis rotations in pitch, roll, and yaw axes (θ, ϕ, ψ). The transformations are performed continuously as the morphing may continuously exhibits motions relative to the frame $\mathcal{F}_B$. The average total processing latency was found to be in the range of 5–7 ms, which is smaller than the sampling interval (16.67 ms).

IV. EXPERIMENTAL RESULTS AND DISCUSSIONS

Finally, we verify the effectiveness of the proposed control approach through real-world experiments on the morphing wing system described in the preceding sections. According to Section III, the system consists of six modules and each of them is driven by two embedded actuators [3]. Without loss of generality, Module 2 is chosen for validation and its adjacent modules are used to produce disturbances. The two control channels of Module 2 are indexed by subscripts 3 and 4, respectively. It is noted that these two channels are identified together, leading to a 2-input-2-output system. The control command and vision feedback data are transmitted at 60 Hz between the host computer (Dell Optiplex 7400 i5-8500 3.0 GHz Processor) and the physical system, while the identifier and the controller work in a host computer at 500 Hz.

First of all, the online identification performance of the incremental model with the RLS algorithm is evaluated. The width of the sliding window is set as $N = 50$, which means 50 previous datasets stored in the host computer is utilized, rather than 50 real samples. The forgetting factor γ_{RLS} is set to be 0.99995 such that the more recent data set has more dominant weight. $\underline{F}_t$, $\underline{G}_t$, and $\underline{\text{Cov}}_t$ are initialized as $\underline{F}_0 = [I_2, 0_{2\times 98}]$, $\underline{G}_0 = [I_2, 0_{2\times 98}]$, and $\underline{\text{Cov}}_0 = 10^3 \cdot I_{200}$, respectively, where $0_{2\times 98}$ denotes the 2-row-98-column matrix with all zero elements.

The identification effectiveness of the incremental model is validated in an open-loop manner using the sinusoidal control input signal, with an amplitude of $A_\delta = 20$ deg, and an angular frequency ω_δ sweeps from 0.2π to 4π rad/s. The identification is activated 1.5 s after the open-loop control process begins. As illustrated in Fig. 5, the predicted displacements converge quickly to their values measured by the vision system as the identification is activated. The identification errors reach the minimum values at around $t = 3$ s, and after that keep increasing as the angular frequency increases. Overall, despite some disturbances and outliers, the identification errors, which are mainly caused by delays, can be bounded within ± 2 deg. The experiment results verify the effectiveness of the incremental model, which makes it suitable for closed-loop control purposes.

Owing to the morphing wing shape sensory limitations reviewed in Section I, feedforward (FF) control currently is and will continue being the mainstream for morphing wings in the near future [48]. Moreover, mechanical imperfections (especially backlash hysteresis) lead to the ineffectiveness of the existing control methods. Therefore, the closed-loop control performance of the IM-NDI control method is evaluated and is compared to the FF control method in the experiment. DIC static measurements are conducted on the top and bottom surface of the morphing modules to assess the capability of the wing demonstrator to attain the static target morphing shapes [49]. A 2×2 FF mapping matrix between the servo angular inputs and the corresponding trailing-edge displacements can accordingly

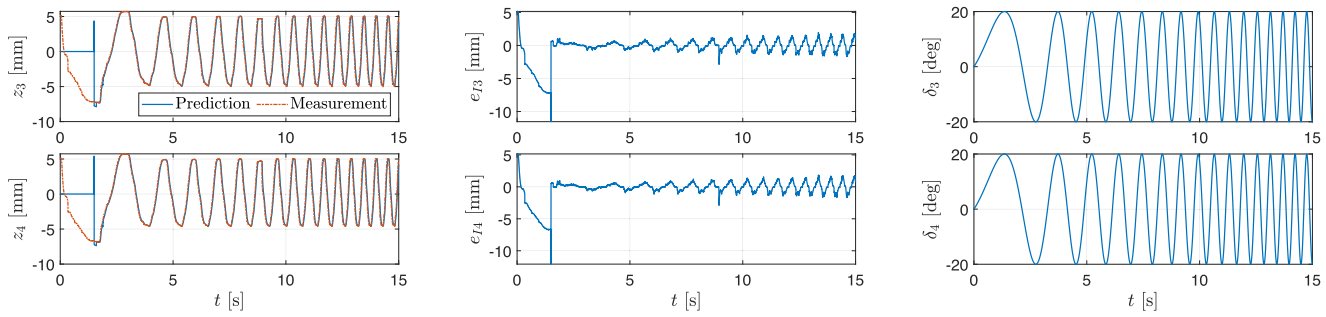

Fig. 5. Open-loop identification performance with a varying-frequency sinusoidal control signal. a) Identification performance. (b) Identification error. (c) Control input.

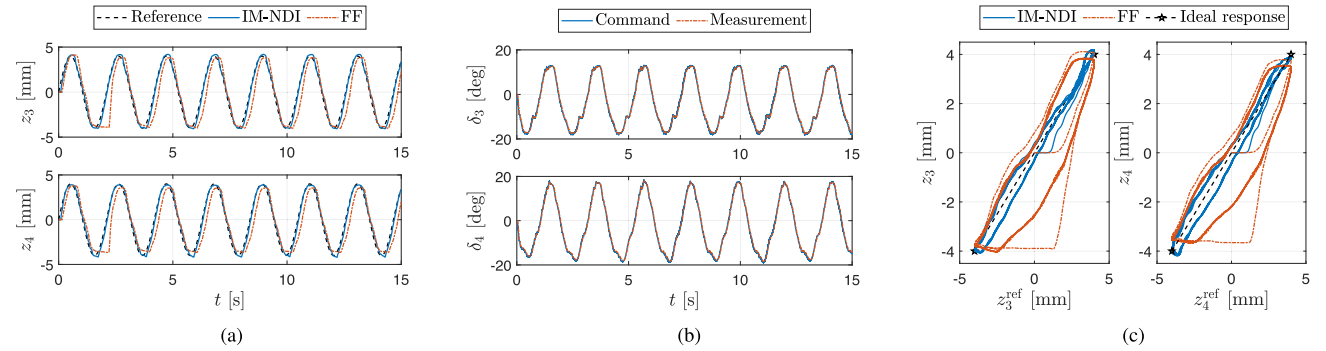

Fig. 6. Control performance when tracking a sinusoidal signal with $\omega = 3$ rad/s and $A_m = 4$ mm. (a) Tracking performance. (b) Control input of IM-NDI. (c) Backlash nonlinearity

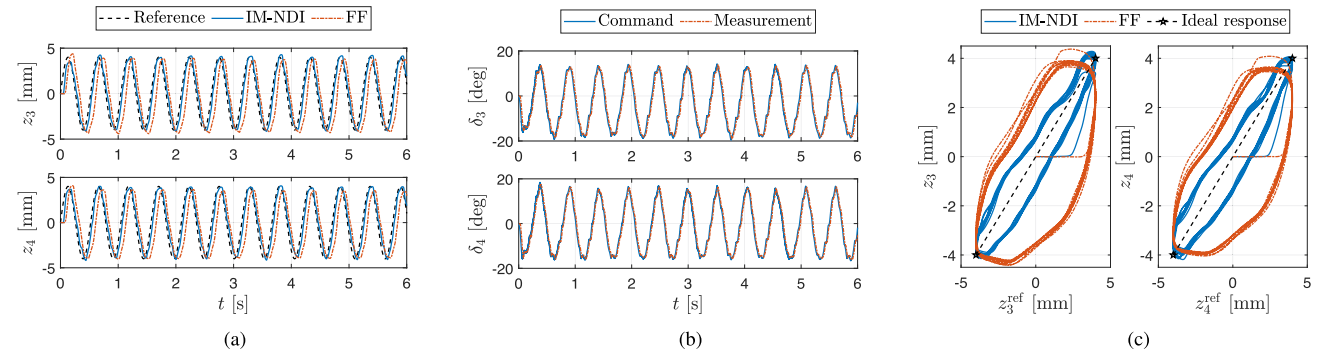

Fig. 7. Control performance when tracking a sinusoidal signal with $\omega = 12$ rad/s and $A_m = 4$ mm. (a) Tracking performance. (b) Control input of IM-NDI. (c) Backlash nonlinearity

be identified. Furthermore, this work extends the result of [49] by measuring the shape-changing caused by discrepant actuator commands within one morphing module such that the nondiagonal elements of the mapping matrix can also be obtained. Then, this mapping matrix is used to directly convert the morphing displacement commands to the servo commands in the FF control cases. For IM-NDI, we experimentally choose $k_p = 22.5$ and $k_d = 1.5$. These gains are tuned considering the tradeoff between tracking error reduction and noise attenuation. The experiments are conducted to track a sinusoidal signal with the same amplitude $A_m = 4$ mm but different angular frequencies. Specifically, the angular frequency ω respectively equals to 3, 6, 9, and 12 rad/s. As representatives, we illustrate the results for $\omega = 3$ rad/s and $\omega = 12$ rad/s in Figs. 6 and 7, respectively. As can be observed, both IM-NDI and FF can successfully track the reference, but IM-NDI has smaller lags and reduced tracking errors.

In Figs. 6 and 7, the control command is the direct output of the IM-NDI controller, while the "measurement" denotes the real angle feedback from the servo. Although small oscillations occur, the actuator shows desirable performance for command tracking. Coping with mechanical imperfections is one of the most challenging issues in this task. Among all mechanical imperfections, backlash is the most dominate and influential nonlinearity in this system, which

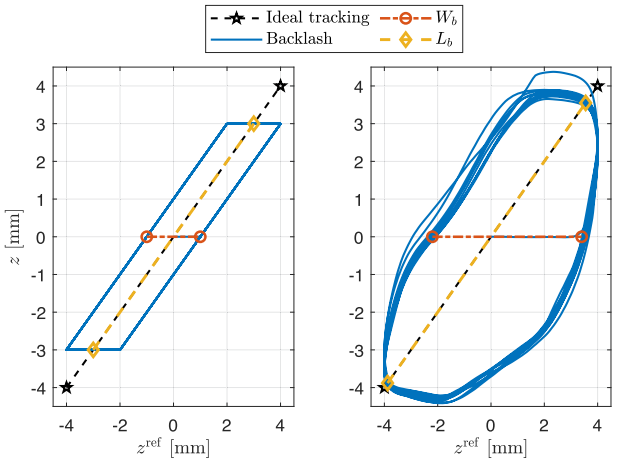

Fig. 8. Illustrative example of the performance metrics for the backlash nonlinearity.

TABLE I
Performance Comparison Regarding the Backlash Compensation, [mm]

	ω [rad/s]	3	6	9	12	Ideal
W_b	FF	2.5050	3.3850	4.5000	5.6000	0
	IM-NDI	0.6250	1.3550	1.9750	2.0750	0
L_b	FF	10.0409	10.1399	10.1823	10.1116	11.3137
	IM-NDI	11.0592	11.0309	10.9743	10.8187	11.3137

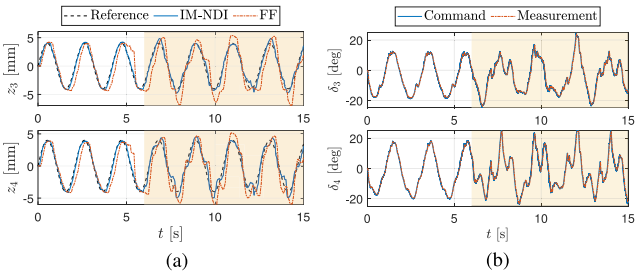

(a) (b)

Fig. 9. Disturbance rejection performance when tracking a sinusoidal signal with $\omega = 3$ rad/s and $A_m = 4$ mm. The shaded area denotes the disturbance injection phase. a) Tracking performance. (b) Control input of IM-NDI.

is also the primary cause for the tracking lag. As illustrated in subfigure (c), the ideal tracking curve is a line segment defined on $[-4, 4]$ mm with a slope of 1. Owing to backlash, the sinusoidal reference and the real measurement make up of a circle curve. It is clear that IM-NDI outperforms the FF controller in handling backlash nonlinearity because the curve of IM-NDI is closer to the ideal tracking line.

To intuitively compare the two methods, we define two tracking performance metrics regarding the width and length of backlash circle, as presented in Fig. 8. The left plot in Fig. 8 illustrates the standard backlash nonlinearity whose width is 2 mm. The width measurement W_b is defined as the length of the horizontal segment that starts and ends at the backlash curve while passing through the origin. The ideal tracking is denoted by the black dashed line whose endpoints are marked as stars. The backlash curve splits the ideal tracking segment and the length of the middle part is defined as the length measurement L_b. Normally, the width W_b is more widely used for describing backlash than L_b.

However, as can be observed from the right subplot of Fig. 8, the real-world nonlinearity is complex and does not exactly obey the mathematical representation of the standard backlash in [20]. Therefore, both W_b and L_b are used as for assessment in this article. The width measurement W_b intends to describe the lagging property when changing the command direction, and a smaller W_b represents better performance. Moreover, the length measurement L_b can reflect the magnitude shrinking effect, and a larger L_b indicates better performance. Fig. 8 shows that as compared to the standard backlash nonlinearity, the effect caused by the real-world backlash nonlinearity is mainly reflected on the W_b, whereas the magnitude shrinking phenomenon is less severe. The control performance comparison regarding different angular frequencies is summarized in Table I, and the data represent the average value of the two actuation channels. It can be observed that thanks to the active compensation, IM-NDI outperforms FF in both W_b and L_b for all angular frequencies, and even the worst case of IM-NDI is better than the best one of FF.

Finally, the robustness of the proposed IM-NDI to external disturbances is verified. Regarding this seamless morphing wing system, all the distributed morphing modules are connected sequentially via elastomeric skin to reduce drag in flight [4]. Consequently, the morphing modules are not purely independent; deflections of one module have impacts on its adjacent modules. Therefore, without changing the settings of Module 2, we will test the robustness of the controller to the disturbances injected by Modules 1 and 3.

In the experiments, Modules 1 and 3 were actuated in an open-loop manner with sinusoidal inputs. In specific, we design an amplitude of 20 deg, an angular frequency of 5 rad/s and a zero phase for Module 1, as well as an amplitude of 25 deg, an angular frequency of 10 rad/s, and a phase of $\phi = \frac{\pi}{2}$ rad for Module 3. The tracking performance is depicted in Figs. 9–12, where the shadowed area stands for the period that the external disturbances are injected. It is clear that with such large disturbances, the control performance of both methods degrade to certain extents. Nevertheless, through Figs. 9–12, it can be observed that IM-NDI in general manages to track the given reference in spite of disturbances by adjusting its control inputs accordingly whereas the FF controller suffers more from the disturbances because it lacks the ability to adapt. For more quantitative comparisons, the root mean square (rms) of the tracking errors in different situations are presented in Table II. Note that Module 2 has two servos; thus, the numbers presented in Table II are the mean values of the two control channels. It is shown that in all situations, IM-NDI outperforms the FF controller in the rms of tracking errors by more than 62%. For both FF and IM-NDI, the rms of tracking errors is larger when disturbances are injected. Nevertheless, although the rms of tracking errors grows as the angular frequency of the reference signal increases, no matter if disturbances exist or not, IM-NDI manages to constrain the rms of tracking errors to within 0.9 deg.

TABLE II
Comparision of the RMS of Tracking Errors, [deg]

ω [rad/s]	3		6		9		12	
Disturbed	No	Yes	No	Yes	No	Yes	No	Yes
FF	1.17	1.76	1.55	2.19	1.95	2.43	2.37	2.98
IM-NDI	0.34	0.62	0.55	0.74	0.73	0.86	0.84	0.87
Improvement	71.06%	64.78%	64.40%	66.34%	62.61%	64.69%	64.69%	70.82%

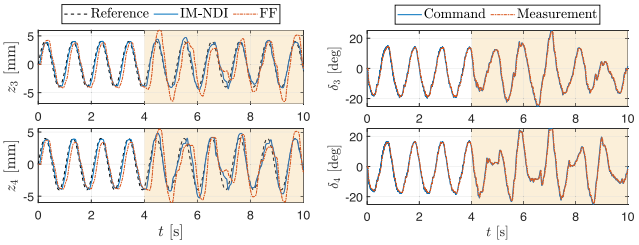

Fig. 10. Disturbance rejection performance when tracking a sinusoidal signal with $\omega = 6$ rad/s and $A_m = 4$ mm. The shaded area denotes the disturbance injection phase. a) Tracking performance. (b) Control input of IM-NDI.

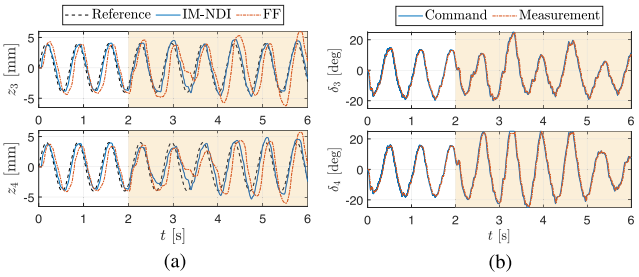

Fig. 11. Disturbance rejection performance when tracking a sinusoidal signal with $\omega = 9$ rad/s and $A_m = 4$ mm. The shaded area denotes the disturbance injection phase. a) Tracking performance. (b) Control input of IM-NDI.

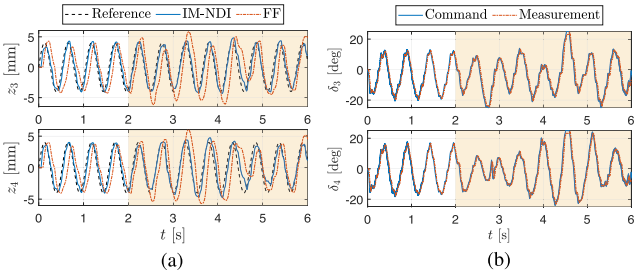

Fig. 12. Disturbance rejection performance when tracking a sinusoidal signal with $\omega = 12$ rad/s and $A_m = 4$ mm. The shaded area denotes the disturbance injection phase. a) Tracking performance. (b) Control input of IM-NDI.

Furthermore, the distributions of tracking errors under different conditions are illustrated in Fig. 13. It can be observed that because of the physically limited servo bandwidth, for both FF and IM-NDI, the standard deviation of tracking errors is increasing as the angular frequency of the reference signal increases. In spite of this, IM-NDI always shows a more clustering property around 0 as compared to FF. When disturbances exist, both methods present a

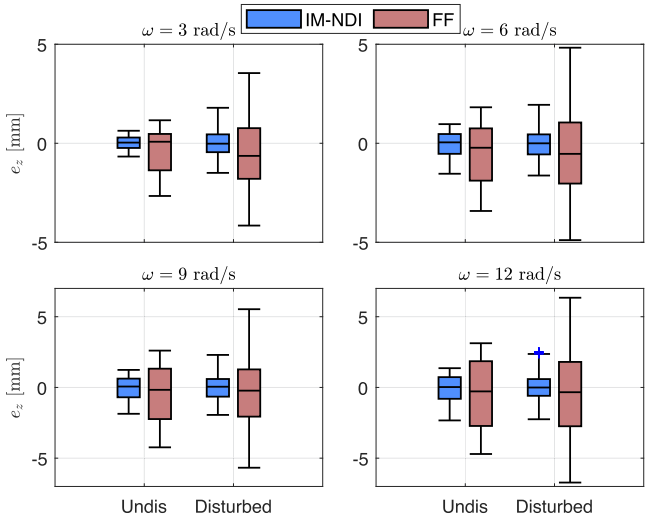

Fig. 13. Distribution of tracking errors under disturbed and undisturbed conditions.

more scattered distribution, but FF shows a more disturbed distribution, which is compatible with the results shown in Figs. 9–12 and Table II. Besides, the mean values of the tracking errors for FF have values further away from 0, whereas IM-NDI still has almost 0 mean values. Magnifying the control gains of IM-NDI (k_p, k_d) can potentially further reduce the data spreads, which however will amplify measurement noise as a side effect. Overall, the results collectively validate the better robustness of the IM-NDI method towards external disturbances.

V. CONCLUSION

Targeting for handling the mechanical imperfections in a seamless active morphing wing, this article develops a data-driven IM-NDI control approach by integrating an online identified IM and the NDI control technique. The system dynamics is identified online merely using the stored input-output data without a prior-known model. Then, an NDI controller is developed based on the identified dynamics.

A crucial aspect of improving these imperfections is an accurate knowledge of the morphing wings' shape. A vision-based control system was developed, which has shown to be adequately effective for this task, given its robustness, high frame rates (250 FPS), and good calibration accuracy (average 0.25 mm). To evaluate the proposed method, a real-world experiment is conducted based on

computer vision feedback. The experimental results demonstrate that by applying the IM-NDI, the morphing wing can track reference signals with different frequencies in spite of external disturbances. Under FF control, the morphing wing suffers from mechanical imperfections, reflected by the lagging and magnitude shrinking phenomena in the tracking responses. The performance of FF control also degrades in the presence of external disturbances. By contrast, experimental results show that IM-NDI can effectively decrease the tracking errors by more than 62% despite disturbances. Furthermore, the proposed vision-based system combined with the control methodology demonstrates the ability to compensate for mechanical imperfections without changing the morphing hardware. All results collectively illustrate the effectiveness of the proposed IM-NDI in dealing with mechanical imperfections existing in the morphing wing system.

APPENDIX A
PROOF OF LEMMA 1

Recalling (5) and (6), the following approximation holds:

$$\begin{aligned}\tilde{A}_{t-2,t-N-1}\Delta x_{t-N} &= \bar{N}V_N\Delta x_{t-N}\\ &\approx \bar{N}\overline{\Delta y}_{t,N} - \bar{N}T_N\overline{\Delta u}_{t-1,N}.\end{aligned} \tag{24}$$

Substituting (8) into (24) yields

$$\begin{aligned}(\bar{N}_0+\bar{N}_1)V_N\Delta x_{t-N} &\approx (\bar{N}_0+\bar{N}_1)\overline{\Delta y}_{t,N}\\ &\quad -(\bar{N}_0+\bar{N}_1)T_N\overline{\Delta u}_{t-1,N}.\end{aligned} \tag{25}$$

It is noted that $\bar{N}_1V_N = 0$, and therefore, $\bar{N}\bar{V}_N\Delta x_{t-N} = \bar{N}_0V_N\Delta x_{t-N}$. Consequently,

$$\begin{aligned}\tilde{A}_{t-2,t-N-1}\Delta x_{t-N} &= \bar{N}_0V_N\Delta x_{t-N}\\ &\approx \bar{N}_0\overline{\Delta y}_{t,N} - \bar{N}_0T_N\overline{\Delta u}_{t-1,N}\end{aligned} \tag{26}$$

independently of $\bar{N}_1$.

By substituting (26) into (5), it can be obtained that

$$\Delta x_t \approx \bar{N}_0\overline{\Delta y}_{t,N} + (U_N - \bar{M}_0T_N)\overline{\Delta u}_{t-1,N} \tag{27}$$

which expresses the incremental state in terms of past input-output data. This completes the proof.

APPENDIX B
PROOF OF THEOREM 2

Since the optimal matrix $\underline{\Theta}$ is valid over $\mathscr{A}$, the previous measurements can uniformly be written as

$$\Delta Y_{t+1}^{\mathsf{T}} = \overline{Z}_t^{\mathsf{T}}\underline{\Theta} + E_{o,t} \tag{28}$$

where $\Delta Y_{t+1} = [\Delta y_{t_0+1}, \ldots, \Delta y_{t+1}] \in \mathbb{R}^{p\times(t-t_0)}$, $\overline{Z}_t = [\overline{z}_{t_0}, \ldots, \overline{z}_t]$, and $E_{o,t} = [e_{o,t_0}, \ldots, e_{o,t}]$. If Assumption 4 holds, $\overline{Z}_t\overline{Z}_t^{\mathsf{T}}$ is guaranteed positive definite and the estimation covariance matrix $\underline{\mathrm{Cov}}_t$ is invertible as $\underline{\mathrm{Cov}}_t^{-1} = \overline{Z}_t\Gamma_t\overline{Z}_t^{\mathsf{T}}$, where $\Gamma_t = \mathrm{diag}([\gamma_{\mathrm{RLS}}^{t-t_0}, \gamma_{\mathrm{RLS}}^{t-t_0-1}, \ldots, 1])$, and $\mathrm{diag}(\cdot)$ reshapes the vector to a diagonal matrix. The approximate matrix $\underline{\hat{\Theta}}_t$ can accordingly be represented as [38]

$$\underline{\hat{\Theta}}_t = \underline{\Theta} + \underline{\tilde{\Theta}}_t = \underline{\Theta} + \underline{\mathrm{Cov}}_t\overline{Z}_t\Gamma_tE_{o,t} \tag{29}$$

where $\underline{\tilde{\Theta}}_t$ denotes the approximation error.

Therefore, the aim of the RLS algorithm is to let the following approximate error correlation matrix converge to 0:

$$\hat{L}_t = E(\underline{\tilde{\Theta}}_t\underline{\tilde{\Theta}}_t^{\mathsf{T}}) \tag{30}$$

where $E(\cdot)$ is the expectation operation. By substituting (29) into (30), and noticing that both $\underline{\mathrm{Cov}}_t$ and Γ_t are symmetrical matrices, we attain

$$\hat{L}_t = E\left(\underline{\mathrm{Cov}}_t\overline{Z}_t\Gamma_tE_{o,t}E_{o,t}^{\mathsf{T}}\Gamma_t\overline{Z}_t^{\mathsf{T}}\underline{\mathrm{Cov}}_t\right). \tag{31}$$

According to Assumption 5, $e_{o,t}$ is the white noise independent of $\overline{z}_t$ such that (31) continues as

$$\begin{aligned}\hat{L}_t &= E\left(\underline{\mathrm{Cov}}_t\overline{X}_t\Gamma_tE(E_{o,t}E_{o,t}^{\mathsf{T}})\Gamma_t\overline{X}_t^{\mathsf{T}}\underline{\mathrm{Cov}}_t\right)\\ &= \sigma_o^2E\left(\underline{\mathrm{Cov}}_t\underline{\mathrm{Cov}}_{2,t}^{-1}\underline{\mathrm{Cov}}_t\right)\end{aligned} \tag{32}$$

where σ_o^2 is the variance of $e_{o,t}$, and $\underline{\mathrm{Cov}}_{2,t}^{-1} = \overline{X}_t\Gamma_t^2\overline{X}_t^{\mathsf{T}}$.

Considering the difficulty in the rigorous evaluation of (32), we approximately evaluate $\hat{L}_t$ with the facilitation of Assumption 5. By noticing that $\underline{\mathrm{Cov}}_t^{-1}$ is a weighted sum of the outer products $\overline{z}_t\overline{z}_t^{\mathsf{T}}$, …, $\overline{z}_{t_0}\overline{x}_{t_0}^{\mathsf{T}}$, the following approximation holds in terms of Assumption 5:

$$\underline{\mathrm{Cov}}_t^{-1} \approx \frac{1-\gamma_{\mathrm{RLS}}^{t-t_0+1}}{1-\gamma_{\mathrm{RLS}}}E_o \tag{33}$$

where $E_o = E(\overline{z}_t\overline{z}_t^{\mathsf{T}})$ is the correlation matrix of measurements. Based on Assumption 4, $\overline{z}_t\overline{z}_t^{\mathsf{T}}$ is positive definite and E_o is invertible.

Substituting (33) into (32) yields

$$\begin{aligned}\hat{L}_t &\approx \sigma_o^2\left(\frac{1-\gamma_{\mathrm{RLS}}}{1-\gamma_{\mathrm{RLS}}^{t-t_0+1}}\right)^2\cdot\frac{1-\gamma_{\mathrm{RLS}}^{2(t-t_0+1)}}{1-\gamma_{\mathrm{RLS}}^2}E_o^{-1}\\ &= \sigma_o^2\frac{1-\gamma_{\mathrm{RLS}}}{1+\gamma_{\mathrm{RLS}}}\cdot\frac{1+\gamma_{\mathrm{RLS}}^{t-t_0+1}}{1-\gamma_{\mathrm{RLS}}^{t-t_0+1}}E_o^{-1}.\end{aligned} \tag{34}$$

In the steady domain, i.e., $t \to M \to \infty$, we obtain that

$$\hat{L}_M = \sigma_o^2\frac{1-\gamma_{\mathrm{RLS}}}{1+\gamma_{\mathrm{RLS}}}E_o^{-1}. \tag{35}$$

It can be observed that if γ_{RLS} is very close to 1, then $\hat{L}_M \to 0$, indicating that the approximate extended matrix converges to the optimal matrix, which ends the proof.

REFERENCES

[1] T. A. Weisshaar
Morphing aircraft systems: Historical perspectives and future challenges
J. Aircr., vol. 50, no. 2, pp. 337–353, Mar. 2013.

[2] R. De Breuker *et al.*
Overview of the SmartX wing technology integrator submitted for publication.

[3] T. Mkhoyan, N. R. Thakrar, R. De Breuker, and J. Sodja
Design of a smart morphing wing using integrated and distributed trailing edge camber morphing
in *Proc. Smart Materials, Adaptive Structures Intell. Syst.*, vol. 84027. American Society of Mechanical Engineers, 2020, Art. no. V001T04A023.

[4] X. Wang, T. Mkhoyan, I. Mkhoyan, and R. De Breuker
Seamless active morphing wing simultaneous gust and maneuver load alleviation
J. Guid., Control, Dyn., vol. 44, no. 9, pp. 1649–1662, 2021.

[5] Q. Shen, D. Wang, S. Zhu, and K. Poh
Finite-time fault-tolerant attitude stabilization for spacecraft with actuator saturation
IEEE Trans. Aerosp. Electron. Syst., vol. 51, no. 3, pp. 2390–2405, Jul. 2015.

[6] N. Vafamand, M. H. Asemani, A. Khayatiyan, M. H. Khooban, and T. Dragičević
TS fuzzy model-based controller design for a class of nonlinear systems including nonsmooth functions
IEEE Trans. Syst., Man, Cybern. Syst., vol. 50, no. 1, pp. 233–244, Jan. 2020.

[7] Z. Lin, S. Lin, S. Wu, G. Ma, and Z. Liang
Vibration control of a flexible spacecraft system with input backlash
IEEE Access, vol. 7, pp. 87017–87026, 2019.

[8] L. Sanches, T. A. Guimarães, and F. D. Marques
Aeroelastic tailoring of nonlinear typical section using the method of multiple scales to predict post-flutter stable LCOs
Aerosp. Sci. Technol., vol. 90, pp. 157–168, 2019.

[9] X. Wang, E.-J. van Kampen, Q. Chu, and P. Lu
Stability analysis for incremental nonlinear dynamic inversion control
J. Guid., Control, Dyn., vol. 42, no. 5, pp. 1116–1129, 2019.

[10] R. R. Selmic and F. L. Lewis
Neural net backlash compensation with Hebbian tuning using dynamic inversion
Automatica, vol. 37, no. 8, pp. 1269–1277, 2001.

[11] B. K. Dinh, M. Xiloyannis, L. Cappello, C. W. Antuvan, S.-C. Yen, and L. Masia
Adaptive backlash compensation in upper limb soft wearable exoskeletons
Robot. Auton. Syst., vol. 92, pp. 173–186, 2017.

[12] L. Acho, F. Ikhouane, and G. Pujo
Robust control design for mechanisms with backlash
J. Control Eng. Technol., vol. 3, no. 4, pp. 175–180, 2013.

[13] H. H. Nguyen and S. Arunsawatwong
Robust controller design for feedback systems with uncertain backlash and plant uncertainties subject to inputs satisfying bounding conditions
IFAC Proc. Volumes, vol. 47, no. 3, pp. 1643–1648, 2014.

[14] Y.-C. Lai and T.-Q. Le
Adaptive learning-based observer with dynamic inversion for the autonomous flight of an unmanned helicopter
IEEE Trans. Aerosp. Electron. Syst., vol. 57, no. 3, pp. 1803–1814, Jun. 2021.

[15] L. Ye, Q. Zong, J. L. Crassidis, and B. Tian
Output-redefinition-based dynamic inversion control for a non-minimum phase hypersonic vehicle
IEEE Trans. Ind. Electron., vol. 65, no. 4, pp. 3447–3457, Apr. 2018.

[16] Y. Huang, D. M. Pool, O. Stroosma, and Q. Chu
Long-stroke hydraulic robot motion control with incremental nonlinear dynamic inversion
IEEE/ASME Trans. Mechatronics, vol. 24, no. 1, pp. 304–314, Feb. 2019.

[17] S.-M. Yoon, W.-H. Choi, and M.-C. Lee
Backlash compensation by smooth backlash inverse for haptic master device using cable-conduit
in *Proc. IEEE 14th Int. Conf. Control, Automat. Syst.*, 2014, pp. 127–132.

[18] K.-H. Han, G.-O. Koh, J.-M. Sung, and B.-S. Kim
Adaptive control approach for improving control systems with unknown backlash
in *Proc. IEEE 11th Int. Conf. Control, Automat. Syst.*, 2011, pp. 1919–1923.

[19] A. Adeleke and J. Mattila
Adaptive backlash inverse augmented virtual decomposition control of a hydraulic manipulator
in *Proc. IEEE Int. Conf. Cybern. Intell. Syst. IEEE Conf. Robot., Automat. Mechatronics*, 2017, pp. 322–327.

[20] R. R. Selmic and F. L. Lewis
Backlash compensation in nonlinear systems using dynamic inversion by neural networks
Asian J. Control, vol. 2, no. 2, pp. 76–87, 2000.

[21] G. Lai, Z. Liu, Y. Zhang, and C. P. Chen
Adaptive fuzzy tracking control of nonlinear systems with asymmetric actuator backlash based on a new smooth inverse
IEEE Trans. Cybern., vol. 46, no. 6, pp. 1250–1262, Jun. 2016.

[22] A. Roudbari and F. Saghafi
Generalization of ANN-based aircraft dynamics identification techniques into the entire flight envelope
IEEE Trans. Aerosp. Electron. Syst., vol. 52, no. 4, pp. 1866–1880, Aug. 2016.

[23] S. A. Emami and A. Roudbari
Multimodel ELM-based identification of an aircraft dynamics in the entire flight envelope
IEEE Trans. Aerosp. Electron. Syst., vol. 55, no. 5, pp. 2181–2194, Oct. 2019.

[24] B. Sun and E.-J. van Kampen
Intelligent adaptive optimal control using incremental model-based global dual heuristic programming subject to partial observability
Appl. Soft Comput., vol. 103, 2021, Art. no. 107153.

[25] Y. Zhou, E.-J. van Kampen, and Q. Chu
Nonlinear adaptive flight control using incremental approximate dynamic programming and output feedback
J. Guid., Control, Dyn., vol. 40, no. 2, pp. 493–496, 2016.

[26] B. Sun and E.-J. van Kampen
Incremental model-based heuristic dynamic programming with output feedback applied to aerospace system identification and control
in *Proc. IEEE Conf. Control Technol. Appl.*, 2020, pp. 366–371.

[27] B. S. Alhayani *et al.*
Visual sensor intelligent module based image transmission in industrial manufacturing for monitoring and manipulation problems
J. Intell. Manuf., vol. 32, no. 2, pp. 597–610, 2021.

[28] T. Mkhoyan, C. C. de Visser, and R. De Breuker
Adaptive real-time clustering method for dynamic visual tracking of very flexible wings
J. Aerosp. Inf. Syst., vol. 18, no. 2, pp. 58–79, 2021.

[29] E. Pan, X. Liang, and W. Xu
Development of vision stabilizing system for a large-scale flapping-wing robotic bird
IEEE Sensors J., vol. 20, no. 14, pp. 8017–8028, Jul. 2020.

[30] S. Tijmons, G. C. De Croon, B. D. Remes, C. De Wagter, and M. Mulder
Obstacle avoidance strategy using onboard stereo vision on a flapping wing MAV
IEEE Trans. Robot., vol. 33, no. 4, pp. 858–874, Aug. 2017.

[31] P. Serra, R. Cunha, T. Hamel, C. Silvestre, and F. Le Bras
Nonlinear image-based visual servo controller for the flare maneuver of fixed-wing aircraft using optical flow
IEEE Trans. Control Syst. Technol., vol. 23, no. 2, pp. 570–583, Mar. 2015.

[32] D. Tang, L. Chen, E. Hu, and Z. F. Tian
A novel actuator controller: Delivering a practical solution to realization of active-truss-based morphing wings
IEEE Trans. Ind. Electron., vol. 63, no. 10, pp. 6226–6237, Oct. 2016.

[33] M. Y. Moemen, H. Elghamrawy, S. N. Givigi, and A. Noureldin
3-D reconstruction and measurement system based on multi-mobile robot machine vision
IEEE Trans. Instrum. Meas., vol. 70, 2021, Art no. 5003109.

[34] Y. Wang, M. Shan, Y. Yue, and D. Wang
Vision-based flexible leader-follower formation tracking of multiple nonholonomic mobile robots in unknown obstacle environments
IEEE Trans. Control Syst. Technol., vol. 28, no. 3, pp. 1025–1033, May 2020.

[35] B. Sun and E.-J. van Kampen
Reinforcement learning-based adaptive optimal flight control with output feedback and input constraints
J. Guid., Control Dyn., vol. 44, no. 9, pp. 1685–1691, 2021.

[36] F. L. Lewis and K. G. Vamvoudakis
Reinforcement learning for partially observable dynamic processes: Adaptive dynamic programming using measured output data
IEEE Trans. Syst., Man, Cybern., Part B. (Cybern.), vol. 41, no. 1, pp. 14–25, Feb. 2011.

[37] N. T. Nguyen
Model-Reference Adaptive Control—A Primer. Berlin, Germany: Springer Int. Publ., 2018, no. 1.

[38] B. Farhang-Boroujeny
Adaptive Filters: Theory and Applications, 2nd ed. Hoboken, NJ, USA: Wiley, 2013.

[39] X. Wang, E.-J. v. Kampen, Q. Chu, and P. Lu
Incremental sliding-mode fault-tolerant flight control
J. Guid., Control, Dyn., vol. 42, no. 2, pp. 244–259, 2019.

[40] QT Brightek
QBLP670-IR3 3528 PLCC2 IR LED
2021.

[41] OptiTrack Primex 41—In depth
Accessed: Jul. 15, 2021. [Online]. Available: https://optitrack.com/cameras/primex-41/

[42] R. Acharya
Multidimensional Image Analysis and Mathematical Morphology. New York, NY, USA: Academic, 1989.

[43] B. Fu *et al.*
High-precision multicamera-assisted Camera-IMU calibration: Theory and method
IEEE Trans. Instrum. Meas., vol. 70, 2021, Art no. 1004117.

[44] K. Kanatani, Y. Sugaya, and Y. Kanazawa
Multiview triangulation
pp. 133–147, 2016. [Online]. Available: https://link.springer.com/chapter/10.1007/978-3-319-48493-8_10

[45] R. Hartley and F. Kahl
Optimal algorithms in multiview geometry
in *Proc. Asian Conf. Comput. Vis.*, 2007, pp. 13–34.

[46] OptiTrack Motive API NaturalPoint product documentation ver 2.2
Accessed: Jul. 15, 2021. [Online]. Available: https://v22.wiki.optitrack.com/index.php?title=Motive_API

[47] A. M. Aurand, J. S. Dufour, and W. S. Marras
Accuracy map of an optical motion capture system with 42 or 21 cameras in a large measurement volume
J. Biomech., vol. 58, pp. 237–240, 2017.

[48] D. Li *et al.*
A review of modelling and analysis of morphing wings
Prog. Aerosp. Sci., vol. 100, pp. 46–62, 2018.

[49] T. Mkhoyan, N. R. Thakrar, R. De Breuker, and J. Sodja
Design and development of a seamless smart morphing wing using distributed trailing edge camber morphing for active control
in *AIAA Scitech 2021 Forum*, pp. 0477–0493, 2021.

Bo Sun (Student Member, IEEE) received the B.Sc. and M.Sc. degrees in aerospace engineering from Northwestern Polytechnical University, Xi'an, China, 2016 and 2019, respectively. He is currently working toward the Ph.D. degree with the Department of Control and Operations, Delft University of Technology, Delft, The Netherlands.

He is currently working on the intelligent controller design for aerial vehicles. His research interests include adaptive dynamic programming, reinforcement learning, and aerospace engineering.

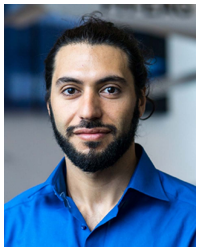

Tigran Mkhoyan (Student Member, IEEE) received the B.Sc. and M.Sc. degrees specializing in advanced control and motion cueing for dynamic flight simulation from the Department of Control and Operations, Delft University of Technology, where he is currently finalizing the Ph.D. degree with the Department of Aerospace Structures and Materials, Faculty of Aerospace Engineering, working on the Smart-X project, an autonomous smart morphing wing.

He is determined to bridge the gap between aeroelasticity, design, and advanced control and push the advancements in aircraft technology toward a new generation of smart aircraft.

Erik-Jan van Kampen received the B.Sc. degree in aerospace engineering, the M.Sc. degree in control and simulation, and the Ph.D. degree in aerospace engineering from the Delft University of Technology, Delft, The Netherlands, in 2004, 2006, and 2010, respectively.

He is currently an Assistant Professor with the Control and Simulation Division, Delft University of Technology. His current research interests include intelligent flight control, adaptive control, and interval optimization.

Roeland De Breuker received the Ph.D. degree in aerospace engineering from the Delft University of Technology, Delft, The Netherlands, in 2011.

In 2011, he joined the Faculty of Aerospace Engineering, Delft University of Technology, as an Assistant Professor and became Associate Professor in 2017. He has been a Visiting Researcher with the Clarkson University, USA, and a Visiting Professor with Airbus Innovations, Germany. He graduated 12 Ph.D. researchers and 69 M.Sc. researchers. He holds 32 journal and 58 conference papers and two patents.

Dr. De Breuker is currently an Associate Fellow of the American Institute of Aeronautics and Astronautics. He is also an Associate Editor for the *Journal of Fluids and Structures* and *Journal of Intelligent Material Systems and Structures*.

Xuerui Wang (Member, IEEE) received the B.S. degree from the Beijing University of Aeronautics and Astronautics, Beijing, China, in 2014, and the Ph.D. degree from Delft University of Technology (TU Delft), Delft, The Netherlands, in 2019, both in aerospace engineering.

From May 2019 to May 2020, she was a Postdoctoral Researcher with the Smart and Aeroelastic Structure Laboratory, TU Delft. Since May 2020, she has been an Assistant Professor with the Faculty of Aerospace Engineering, TU Delft. Her tenure track program is cofunded by the Department of Control and Operations and the Department of Aerospace Structures and Materials. Her research interests include nonlinear control, aeroelasticity, aerial robotics, and active morphing structures.